APPLIED SCIENCES AND ENGINEERING

Bioinspired tough gel sheath for robust and versatile surface functionalization

Zhenwei Ma[1], Zhen Yang[1], Qiman Gao[2], Guangyu Bao[1], Amin Valiei[3], Fan Yang[4], Ran Huo[1], Chen Wang[4], Guolong Song[4], Dongling Ma[4], Zu-Hua Gao[5], Jianyu Li[1,6,7]*

Sutures pervade surgeries, but their performance is limited by the mechanical mismatch with tissues and the lack of advanced functionality. Existing modification strategies result in either deterioration of suture's bulk properties or a weak coating susceptible to rupture or delamination. Inspired by tendon endotenon sheath, we report a versatile strategy to functionalize fiber-based devices such as sutures. This strategy seamlessly unites surgical sutures, tough gel sheath, and various functional materials. Robust modification is demonstrated with strong interfacial adhesion (>2000 J m^{-2}). The surface stiffness, friction, and drag of the suture when interfacing with tissues can be markedly reduced, without compromising the tensile strength. Versatile functionalization of the suture for infection prevention, wound monitoring, drug delivery, and near-infrared imaging is then presented. This platform technology is applicable to other fiber-based devices and foreseen to affect broad technological areas ranging from wound management to smart textiles.

INTRODUCTION

Sutures are a class of fiber-based devices primarily to mechanically approximate tissues or attach wearable/implantable devices to human body (*1*). They are in the form of either mono- or multifilaments (i.e., braided) and designed to degrade or stay permanently in the body. A variety of materials have been invented and adopted as surgical sutures, including plastics (degradable: polyglycolide and polylactic acid; nondegradable: nylon and polypropylene), biologically derived proteins (collagen and silk), and metals (stainless steel and nitinol). The sutures have been widely used in many branches of medicine such as wound closure and anastomosis with a global market of over 5 billion U.S. dollars (*2*). Despite the recent progress of tissue adhesives (*3*–*7*), they will remain indispensable for general surgical procedures because of their reliable performance, ease of implementation, and the capacity to exert larger forces than any tissue adhesives (*2*).

However, the performance of existing sutures has been limited by their poor biomechanical properties and lack of functionality, which are implicated in surgical and postsurgical complications. First, sutures are made of rigid dry materials (elastic modulus of >1 GPa) in contrast to soft hydrated tissues (elastic modulus of <100 kPa), as they need to carry substantial mechanical loading along the axis to approximate tissues (*8*). This mechanical mismatch is found to cause inflammation and impaired healing outcomes (*9*). Second, the rough surface of sutures, particularly for the braided sutures, can drag and rub against the contacting tissue during and after suture placement. This mechanical irritation can damage fragile tissues and those under disease conditions such as aneurysm and ulcer, leading to tissue dissection and other postsurgery complications (*10*, *11*). In addition, clinically used sutures lack advanced functionality for wound management. Thus, multifunctional sutures are in demand to perceive, report, and respond to the wound healing process, for instance, delivering therapeutic to promote wound healing (*12*) and preventing surgical site infections (*13*). These functional sutures are developed recently, which feature drug delivery or sensing capacities. There are also drug-eluting or antibacterial sutures commercially available (e.g., Coated VICRYL Plus Antibacterial, Ethicon), capable of releasing drug or antibacterial compounds (*14*). However, limitations to these approaches remain, including complex fabrication process, high cost, limited physical integrity, and the abovementioned biomechanical constraints. These issues associated with surgical sutures are also found in other fiber-based devices, particularly those interfacing with the human body such as guidewires and smart textiles. New strategies to improve the biomechanical properties, functionality of sutures, and other fiber-based devices continue to be sought.

General strategies to functionalize sutures include bulk modification and surface functionalization. The former involves bottom-up approaches to (re)produce the suture (e.g., electrospinning and melt extrusion), which may compromise the suture's strength and are inapplicable to commercially available sutures (*15*, *16*). To minimize the alteration of the bulk properties, the surface functionalization is appealing, which results in a suture coating via dip coating/soaking (*17*, *18*), layer-by-layer deposition (*19*, *20*), grafting (*21*–*23*), and impregnation (*24*, *25*). However, the suture coating is often weak and vulnerable to fragmentation and delamination, due to the chemical inertness of suture materials and the demanding mechanical loading of the suture application (e.g., shear and compression during suturing and knotting). The mechanical failure of suture coating results in the loss of functionality (fig. S1, A to C) and other side effects (e.g., burst drug release for drug-eluting suture coating). Evidently, the toughness and adhesion of the suture coating is thus mission critical and recognized as a prerequisite of any reliable functionalization.

For surface functionalization of surgical sutures, hydrogel technologies are promising in light of recent developments of tough

[1]Department of Mechanical Engineering, McGill University, Montréal, QC H3A 0C3, Canada. [2]Faculty of Dentistry, McGill University, Montréal, QC H3A 1G1, Canada. [3]Department of Chemical Engineering, McGill University, Montréal, QC H3A 0C5, Canada. [4]Institut National de la Recherche Scientifique–Énergie Matériaux et Télécommunications, Université du Québec, Varennes, QC J3X 1S2, Canada. [5]Department of Pathology, McGill University and the Research Institute of McGill University Health Centre, Montréal, QC H4A 3J1, Canada. [6]Department of Biomedical Engineering, McGill University, Montréal, QC H3A 2B4, Canada. [7]Department of Surgery, McGill University, Montréal, QC H3A 2B4, Canada.
*Corresponding author. Email: jianyu.li@mcgill.ca

hydrogel adhesion on various materials such as tissues (*3*), hydrogels (*26*), metals (*27*), and elastomers (*28*). These established strategies exploit preformed hydrogel patches to be applied on flat surfaces and thus are not compatible with fiber-based devices as sutures. Formation of hydrogel coating on complex structures has been recently reported but is focused on single-network hydrogels and elastomer-based devices (*29*). Neither this strategy nor the other methods are applicable on surgical sutures because of the chemical innerness of suture materials. In addition, most adhesive hydrogels are inclusion free and lack advanced functionality. Particularly, few works to date demonstrate wound bed monitoring and near-infrared (NIR) bioimaging applications with hydrogel coatings. Further development is needed to reinvent and repurpose the hydrogel coating for sutures and other fiber-based devices.

To address the abovementioned issues, we report a bioinspired design and fabrication method for multifunctional tough gel–sheathed (TGS) sutures. Different from the previously reported methods based on surface absorption or single-network hydrogels, our strategy features a double-network TGS strongly bonded with surgical sutures for robust modification. The TGS is hypothesized to help mitigate the mechanical mismatch and irritation of sutures when interfacing with tissues and to further provide a robust and versatile platform to functionalize commercially available sutures for advanced functionality. As a proof of principle, motivated by the clinical need of wound management, we will demonstrate the TGS sutures loaded with an antibacterial compound, pH-sensing microparticles, drugs, and fluorescent nanoparticles (NPs) for anti-infection, wound bed monitoring, drug delivery, and NIR bioimaging applications. This work will demonstrate that the TGS suture could unite the merits of suture fibers, tough hydrogels, and functional materials by design and thus achieve a unique combination of enhanced biomechanical properties and multiple functionality, which would be beneficial for general surgical procedures and wound management (fig. S1D).

RESULTS

Design and fabrication of TGS sutures

The design of TGS suture is inspired by endotenon sheath of tendon, which encapsulates and glues collagen fibers together (Fig. 1A) (*30*). The endotenon sheath is mechanically tough and strongly adhesive on the collagen fibers, attributing to its double-network structure: The hyaluronan-proteoglycan network binds with the collagen fibers, while the elastin network strengthens and toughens the whole structure. The endotenon sheath not only forms a frictionless surface of the tendon but also comprises cells and blood vessels for mass transport and repair of the tendon. Learning from the structure and function of the endotenon sheath, we propose a TGS to modify and further functionalize commercially available sutures. To achieve the strong bonding with the suture, the TGS contains one anchoring network that forms covalent bonds on the suture surface for strong adhesion and intertwines with another toughening network consisting of physical bonds, which can effectively dissipate energy for high toughness (general design strategy illustrated in Fig. 1B). This strategy is distinct from the surface absorption, the single-layer polymer grafting, and the hydrogel skin method that requires swelling and doping the substrate with free-radical initiators to form a single-network hydrogel coating (*20*, *23*, *29*).

The TGS sutures are prepared directly from commercially available surgical sutures with a facile two-step method. We illustrate the essential procedure with a widely used braided surgical suture, Coated VICRYL (Ethicon), consisting of polyglactin 910 [copolymer of 90% glycolide and 10% lactide (PLGA)] coated with polyglactin 370 and calcium stearate (*14*), and an alginate-polyacrylamide (PAAm) hydrogel that acts as the TGS because of its high toughness and excellent biocompatibility (*31*). As the pristine suture lacks the functional groups for anchoring, the suture was first treated with 1 M NaOH solution to create carboxylic acid groups on the surface, which was later primed with primary amine–rich chitosan macromolecules and coupling reagents [1-ethyl-3-(-3-dimethylaminopropyl) carbodiimide hydrochloride (EDC) and *N*-hydroxysuccinimide (NHS)] to form the anchoring network. To form the toughening network, we then inserted the modified suture into a glass capillary tube filled with a precursor solution of alginate-PAAm hydrogels; after gelation overnight, the TGS suture was obtained after post–cross-linking in 0.1 M $CaCl_2$ solution (fig. S2). The applicability of this strategy to other hydrogels and suture materials will be presented below. Sutures of a wide range of diameters (0.01 to 1 mm) are used by surgeons in different surgical procedures. Our results demonstrated that the suture was robustly integrated with a thin TGS and that the thickness was tunable with the diameter of the capillary tube (Fig. 1, C to E). With our current setup, we can reproducibly fabricate 10- to 15-cm-long TGS suture threads with consistent coating thickness (fig. S3A). For the long-term storage of TGS sutures, they can be freeze-dried, kept at their dry state as other commercialized sutures, and then simply rehydrated in saline solutions before usage (fig. S3B). As a demonstration of its physical integrity, a continuous stitch with secured knotting was successfully performed on porcine skin using the TGS suture (Fig. 1F). The in vitro biocompatibility of the TGS suture–conditioned medium is comparable to that of the control medium, showing no notable difference in the in vitro viability of human vocal fold fibroblasts after 48-hour culture (fig. S4).

Strong suture-sheath bonding

To interrogate the bonding between the suture and the hydrogel sheath, we invented a pull-out test to characterize the adhesion energy of suture-sheath interface. Briefly, the suture was embedded within a hydrogel cuboid and then pulled out with an Instron machine (model 5965), while the force F and the displacement δ were recorded (fig. S5). The two opposing sides of the hydrogel cuboid were glued to two acrylic sheets as rigid constraints. It was observed that the adhesion survived at a large pull-out displacement (20 mm versus 30 mm of the adhesion interface) and that part of the tough gel matrix still attached to the suture even when it was completely pulled out (Fig. 2A and fig. S5).

An analytical model was developed and applied to calculate the adhesion energy. The strain energy density stored in the hydrogel sheath U_g can be calculated from the force-displacement curve until the point when the interface failed via $U_g = \int F(\delta)\, d\delta/(\pi(r_{tot}^2 - r_s^2)\, L)$, where r_s denotes the suture radius; r_{tot} denotes the summation of the hydrogel sheath thickness r_g and suture radius, i.e., $r_{tot} = r_g + r_s$; L denotes the jointed length. The critical energy release rate, i.e., adhesion energy, was calculated from U_g with the equation (see Materials and Methods for derivation and other details)

$$\Gamma = \frac{U_g(r_{tot}^2 - r_s^2)}{2\, r_s} \quad (1)$$

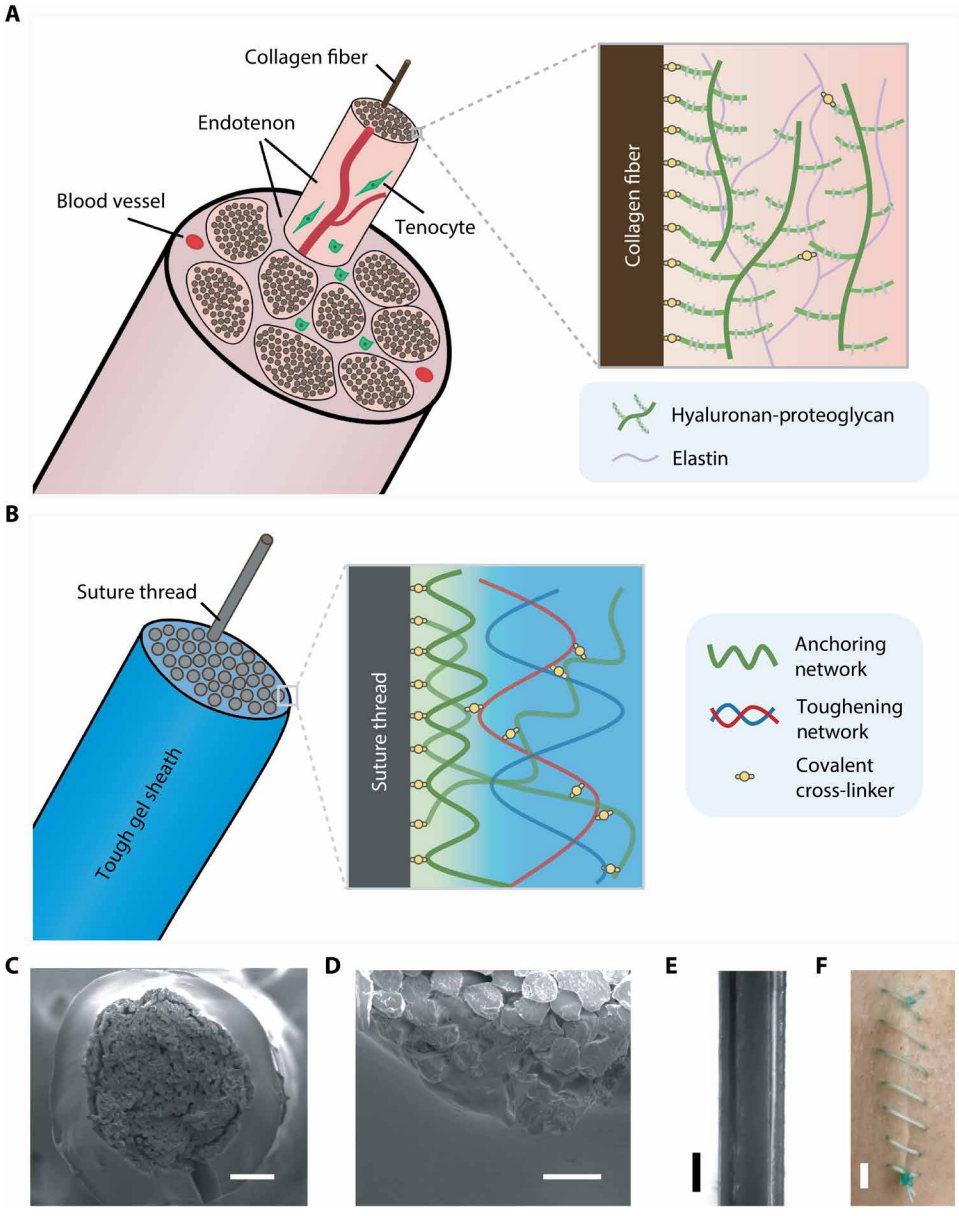

Fig. 1. Bioinspired design of TGS suture. Schematics of the structural and material design of (**A**) tendon and (**B**) TGS suture. Scanning electron microscope images of (**C**) TGS suture and (**D**) a zoom-in at the suture-sheath interface. Scale bars, 100 (C) and 25 μm (D). (**E**) Bright- field image of TGS suture. Scale bar, 500 μm. (**F**) A continuous stitch applied on porcine skin using TGS suture. Scale bar, 1 cm. Photo credit: Zhenwei Ma, McGill University.

With the above equations, we calculated that the adhesion energy obtained from the alginate-PAAm–sheathed polyglactin 910 suture was over 1000 J m^{-2} (Fig. 2B), which was comparable with the tough adhesion of hydrogels achieved on tissues, elastomers, and metals.

To reveal the mechanism for the strong adhesion, we next separately delineated the effects of the anchoring and toughening networks. First, to evaluate the importance of the toughening network, the suture sheath was formed with brittle single-network hydrogels (e.g., alginate or PAAm hydrogels), which largely resembled the strategies reported previously (*17*, *29*). Without a tough matrix, the suture-sheath interface is vulnerable to rupture (adhesion energy of <50 J m^{-2}) (Fig. 2B). Second, to confirm the role of the anchoring network, we fabricated the sheathed sutures without NaOH treatment or surface priming (chitosan/EDC/NHS). Evidently, the lack of strong anchoring network led to very low adhesion energy (<50 J m^{-2}) (fig. S6A). The result also implied that the mechanical interlocking of the hydrogel within the braided suture played a small role. The importance of amide-based interfacial bonds was further confirmed with a positive correlation between the duration of NaOH treatment and the adhesion energy (Fig. 2C). Over 2000 J m^{-2} adhesion energy was achieved with 10-min surface activation. It can be concluded that the strong adhesion is attributed to the synergy of the energy dissipation of the hydrogel matrix and the covalent bonding at the suture-sheath interface. It should be noted that strong adhesion was achieved with the standard coated

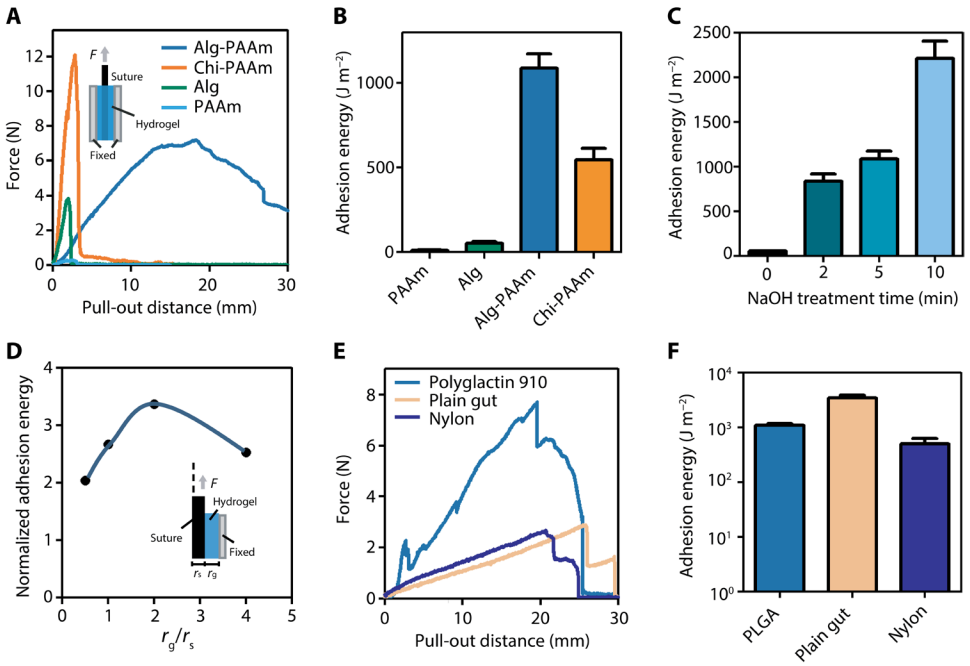

Fig. 2. Strong adhesion of TGS and suture. Representative force-displacement curves (**A**) and the adhesion energy (**B**) measured from the pull-out tests [inset in (A)] of gel-sheathed sutures formed with polyglactin 910 suture and different hydrogels. Alg, alginate; Chi, chitosan. (**C**) Adhesion energy as a function of NaOH treatment time. (**D**) FEM results of the normalized adhesion energy (Γ/Γ_0) as a function of the ratio of the sheath thickness and the suture radius (r_g/r_s). The force-displacement curves of pull-out test (**E**) and the adhesion energy (**F**) of TGS sutures encompassing various suture materials, including polyglactin 910 (PLGA), plain gut, and nylon. Data reported as means ± SD for $n = 3$ independent experiments.

polyglactin 910 sutures. Given the same chemistry of the polyglactin 370 coating and the bulk of the suture filament, similar results are expected for the uncoated versions.

Finite element modeling of suture-sheath adhesion

To further model the interfacial failure mechanism and aid the design of suture sheath, we developed a finite element model (FEM) to simulate the pull-out process of a suture from a hydrogel sheath. The toughening network was characterized with the combined Ogden and modified Ogden-Roxburgh model that accounts for the Mullins effect, while the anchoring network was modeled as cohesive elements with low (24 J m^{-2}) and high (300 J m^{-2}) intrinsic toughness values Γ_0 (*32*). Our simulation showed that the adhesion energy Γ increased with the intrinsic toughness Γ_0 (fig. S6, B and C), consistent with the observation of stronger adhesion after longer NaOH treatment (Fig. 2C). To study the effect of sheath thickness, we varied the hydrogel thickness in terms of normalized hydrogel radius r_g/r_s while keeping the intrinsic toughness $\Gamma_0 = 300$ J m^{-2}. As the adhesion energy Γ is shown to scale linearly with Γ_0 (*33*), we normalized the adhesion energy Γ by the intrinsic toughness Γ_0. Large normalized adhesion energy was observed ($\Gamma/\Gamma_0 > 2$) in all tested conditions (Fig. 2D), indicative of a potent toughening effect of the TGS (*31*). We found a nonmonotonic correlation between Γ/Γ_0 and r_g/r_s. After examining the shear stress distribution along the joint interface, we interpret the observation as follows (fig. S7, A to E). Given a thin sheath ($r_g/r_s \leq 2$), the suture-sheath interface debonds simultaneously, and the volume of energy dissipating materials increases with the thickness of the suture sheath, leading to higher adhesion energy; when the sheath is even thicker, the energy dissipation is confined around the crack tip, and thus, the total amount of dissipated energy is reduced, as well as the adhesion energy.

Wide applicability of TGS design

The design and method for the TGS sutures are applicable to a variety of surgical sutures and hydrogels. Besides the synthetic degradable PLGA suture, we have successfully fabricated the TGS sutures using naturally derived degradable plain gut sutures and synthetic nondegradable nylon sutures (Fig. 2, E and F) with the same method. Furthermore, the suture sheath can be formed with various hydrogels as the toughening network, which can interpenetrate with the chitosan-based anchoring network. As an example, we formed a TGS composed of a chitosan-PAAm hydrogel. The efficacy of our method is evidenced with high adhesion energy of the sheath-suture interfaces in all the tested conditions. This study leads to a family of TGS sutures of varying chemical compositions and properties and demonstrates the versatility of the proposed design and method.

Enhanced biomechanical properties

We next demonstrated that the intrinsic biomechanical properties of TGS sutures could help mitigate the limitations of clinically used suture materials. The core-sheath structure could provide low-stiffness hydrogel surface to resolve the mechanical mismatch between the suture and local tissues, without sacrificing the tensile strength of the pristine sutures for wound closure. With carefully controlled suture hydrolysis via NaOH treatment, the obtained TGS suture retained high tensile strength (3 GPa), comparable to pristine sutures (Fig. 3A and fig. S8). However, prolonged surface treatment will lead to compromised suture strength, despite the enhanced interfacial adhesion (Fig. 2C and fig. S8). The surface elastic modulus of

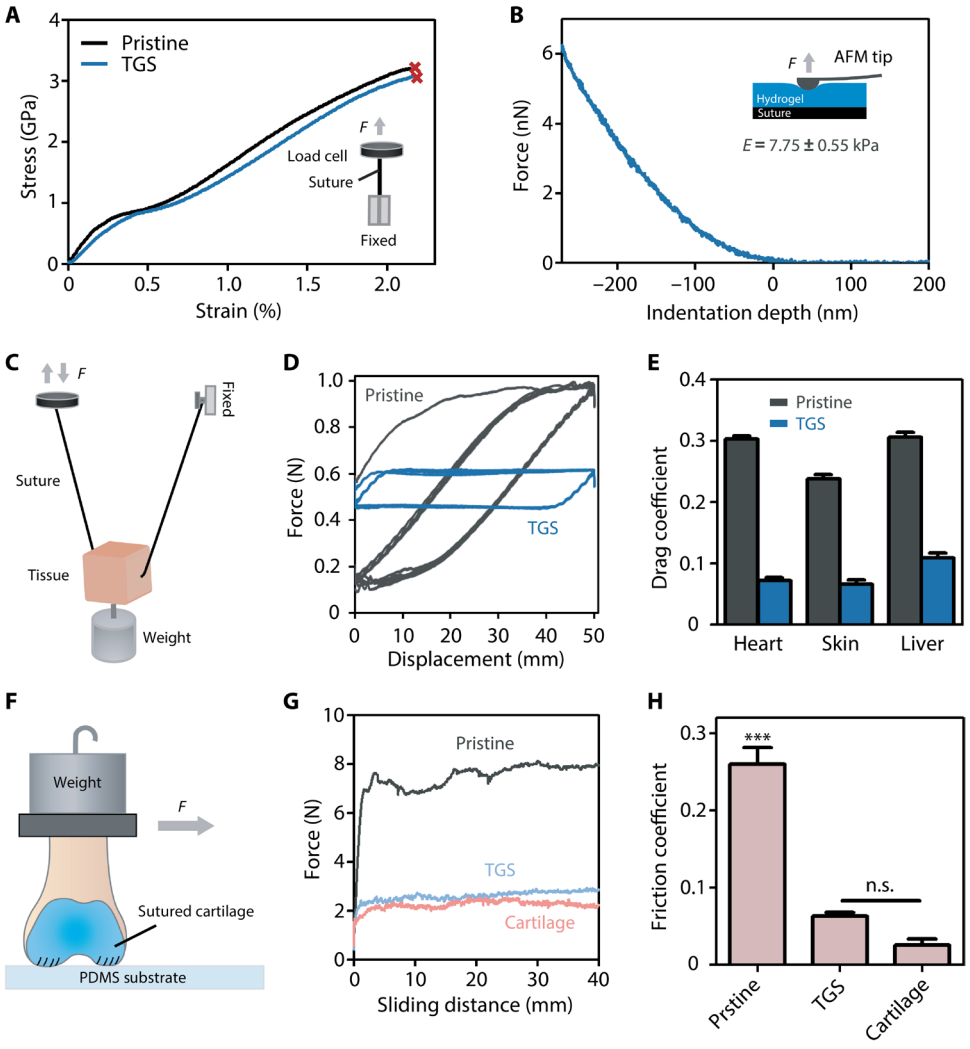

Fig. 3. Improved biomechanical properties of the TGS suture. (**A**) Stress-strain curves of the pristine and TGS sutures (polyglactin 910). (**B**) Representative microindentation force-indentation depth curve measured on the TGS suture surface. AFM, atomic force microscope. (**C**) Schematic of the tissue drag test. (**D**) Representative drag force-displacement curves of the pristine and TGS sutures. (**E**) Drag coefficients of suture (pristine or TGS) interfacing with various tissues (heart, skin, and liver). (**F**) Schematic of the ex vivo friction test of the suture placed on articular cartilage, where the PDMS is used as a substrate. Representative friction force-sliding distance curves (**G**) and the calculated friction coefficients (**H**) of intact cartilage and sutured cartilage with the pristine or TGS suture. Data reported as means ± SD for $n = 3$ independent experiments; ***$P < 0.001$, by two-tailed, one-way analysis of variance (ANOVA) with Holm-Sidak post hoc comparison.

the TGS suture is around 7 kPa measured by atomic force microscopy equipped with a cell-sized spherical probe (Fig. 3B), compared to ultrahigh stiffness of ~68 MPa of the pristine suture (fig. S9). The activation treatment is strictly limited to the very superficial layer of sutures and yet provides sufficient functional groups for binding with the sheath. The mechanical mismatch between the suture and soft tissues is thus remedied by the soft hydrogel sheath, which may also mitigate the local stress concentration and enable a mechanical microenvironment favorable for tissue regeneration.

In addition to the low stiffness, TGS suture also provides a slippery surface when interfacing with the tissues, which could substantially reduce the tissue drag and friction that have been linked with microtrauma and tissue damage (*34*). When passing through the tissue, traditional sutures can drag and damage the tissue; after the placement, the rough surface of sutures, particularly braided ones, can cause constant friction and wear on the contacting tissue. This is particularly severe for tissues under constant friction and impact, such as articular cartilage, where surgical suturing has been associated with higher risk of osteoarthritis (*10*). To characterize the tissue drag, we performed a customized ex vivo drag test, mimicking the suturing process, to determine the drag coefficient of the TGS and pristine sutures on soft tissues such as skin, heart, and liver (Fig. 3, C to E). The results show that the drag coefficients of the TGS sutures are two to three times lower than that of pristine sutures (Fig. 3E). A characteristic stick-and-slip phenomenon was observed in the drag force-displacement profile of the pristine sutures but not in the case of the TGS sutures (Fig. 3D and fig. S10). We also developed a customized setup to characterize the friction induced by the sutures on porcine articular cartilage (Fig. 3F). Using polydimethylsiloxane (PDMS) as an artificial tissue substrate, we characterized the friction coefficient between PDMS and cartilage or sutured cartilage using the pristine or TGS sutures. Our results

show that friction coefficient for TGS sutures was comparable to articular cartilage and significantly lower than the pristine sutures (Fig. 3, G and H).

Versatile functionalization

Besides the excellent biomechanical properties inherent to the TGS, the functionality of the TGS sutures will next be engineered through inclusion of various functional materials. It is feasible as the TGS can serve as a versatile platform, warranted by the robust modification, to readily encapsulate and deliver small payloads along with the suture to the strategic site adjacent to a wound. As a proof of principle, we will load the suture sheath with an antibacterial compound, pH-sensing microparticles, a model drug, and fluorescent NPs and then demonstrate the effectiveness of the functionalization below.

The interfilament spacing within braided sutures may attract bacteria through capillary forces and host bacteria growth. Owing to the cell-repellent nature of PAAm, the TGS suture exhibited excellent antifouling property with significantly lower bacteria adhesion, for both Gram-positive (*Staphylococcus aureus*) and Gram-negative (*Pseudomonas aeruginosa*) bacteria that are closely associated with surgical site infection (Fig. 4, A and B) (*35*). By further loading the TGS with an antibacterial compound [benzalkonium chloride (BZK)] widely used in many consumer products, over 99% of the adhered bacteria were killed (Fig. 4C and fig. S11), thanks to the positively charged quaternary ammonium compound incorporated into the hydrogel matrix (*35*). This study demonstrates the antifouling and antimicrobial functions of the TGS suture and its potential for mitigating surgical site infection.

The suture sheath can be further functionalized to monitor the physiological signals during wound healing processes because of the strategic location of surgical sutures at the wound site. As a proof of concept, we loaded pH-sensing beads into the TGS as pH-monitoring sutures. The wound bed pH is a key indicator of the wound healing process: Healthy skin is often acidic, and for wound bed exposed to body fluid, the pH is usually around 7, while the pH of chronic wounds or infected wounds could go up to 10 (*36*, *37*). Our results show that the pH-sensing sutures readily transduce the pH signal into color change, visible to the naked eye (Fig. 4, D and E). The monitoring could be continuous and essentially minimally invasive as the sutures naturally penetrate through the wounded tissue; the semipermeable hydrogel sheath allows for mass exchange at the molecular level (yet does not allow bacterial invasion). The new suture function would particularly benefit the monitoring of chronic wounds by nonprofessionals and in-time intervention when the pH level is abnormal. By integrating the antifouling and antibacterial functions, the new suture technology could be potentially used as point-of-care systems for the management of chronic wounds.

The TGS suture can also serve as a depot to locally deliver drugs to the wound site. The TGS can encapsulate the drug and regulate its release through the drug-matrix interactions. As a proof of concept, we loaded the TGS with fluorescein isothiocyanate (FITC)–bovine serum albumin (BSA) as a widely used model drug to form drug-eluting TGS sutures. We also dip-coated the pristine suture with the model drug as a control for comparison. A 1-week cumulative release profile shows that TGS suture presents higher encapsulation efficiency and longer release period, compared to the control suture using dip-coating strategy (Fig. 4, F and G). Together with the abovementioned demonstrations, we show that the TGS platform enables the diagnostic, monitoring, and therapeutic functions to address the clinical needs for wound management.

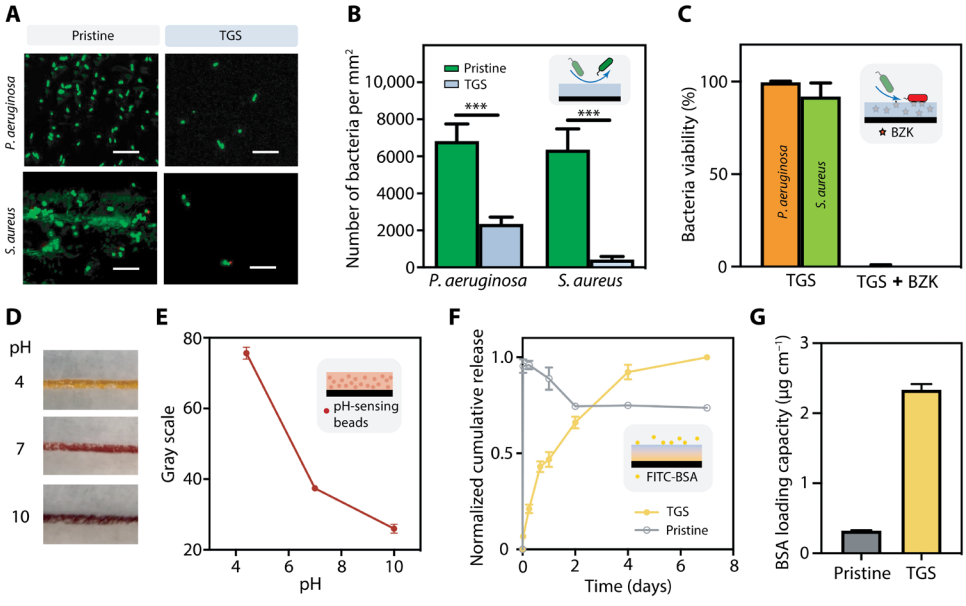

Fig. 4. Versatile TGS suture functionalization. (**A**) Representative fluorescence images of live (green)/dead (red) assay of bacteria (*P. aeruginosa* and *S. aureus*) seeded onto the pristine or TGS suture. Scale bar, 10 μm. (**B**) Total number of bacteria adhesion on pristine or TGS sutures. (**C**) Over 99% bacteria were killed on TGS sutures loaded with BZK. Representative images (**D**) and quantitative color change assay (reflected in gray scale) (**E**) of pH-sensing TGS suture immersed in solution with various pH levels. Photo credit: Zhenwei Ma, McGill University. (**F**) Seven-day normalized cumulative release profile of FITC-BSA from the pristine or TGS suture. (**G**) BSA loading capacity of pristine or TGS suture. Data reported as means ± SD for $n = 3$ independent experiments; ***$P < 0.001$, by two-tailed, one-way ANOVA with Holm-Sidak post hoc comparison.

The intricate surgical procedures and delicate soft tissues call for the precise targeting and visualization of sutures during and after operation. NIR fluorescence imaging is an emerging biomedical imaging modality for use in both fundamental scientific research and clinical practice (*38*). By incorporating our recently developed NIR fluorescent NPs (*39*) (with fluorescence emission wavelength at 1250 nm in NIR-II: 1000 to 1350 nm; Fig. 5, A and B, and fig. S12) into the TGS, we further expand the potential of our platform for deep-tissue bioimaging via a customized ex vivo setup (Fig. 5C). The fluorescent NP–loaded TGS suture exhibits bright linear fluorescence along suture with dark background captured by an NIR camera under excitation of an 806-nm laser in NIR-I (700 to 950 nm), and the strong signal could still be observed when the suture was covered by porcine tissue with up to 3-mm thickness (Fig. 5D). The intense NIR fluorescence and high contrast demonstrate the deep-tissue penetration capability of the fluorescent suture. To our knowledge, this first demonstration of fluorescent sutures with high optical transparency in the NIR biological window would facilitate minimally invasive surgeries to localize the suture during implementation and later removal and benefit fluorescence image-guided surgery and postsurgery bioimaging/diagnostics (*40*).

In vivo biocompatibility

The in vivo biocompatibility of the TGS sutures was evaluated via subcutaneous implantation of the suture knots in rats for 7 and 14 days (Fig. 6A). The pristine sutures were included as comparison. No notable degradations were observed for both pristine and TGS sutures during the 2-week period (Fig. 6B). Histological assessment by an experienced pathologist indicate that the two sutures elicit comparable mild inflammation response on day 7, while the TGS sutures showed very mild to none inflammation on day 14, significantly better than pristine sutures (Fig. 6C and fig. S13). This is evidenced with the elevated cell infiltration into the pristine suture interfilament spacings overtime (Fig. 6, D and E) and the presence of foreign body giant cells and proinflammatory eosinophils within the proximity of pristine suture filaments (Fig. 6, H and I). For the TGS sutures, no foreign body inflammatory reactions were observed on days 7 and 14 (Fig. 6, F and G). A thin capsule with a minimal number of lymphocytes was identified surrounding the TGS suture knot, yet no giant cells, neutrophils, or macrophages were noticed (Fig. 6, J and K). Exhaustive examination revealed no cell infiltration into the TGS sutures because of the nanoporosity of the hydrogel sheath, indicating a good suture-sheath integration.

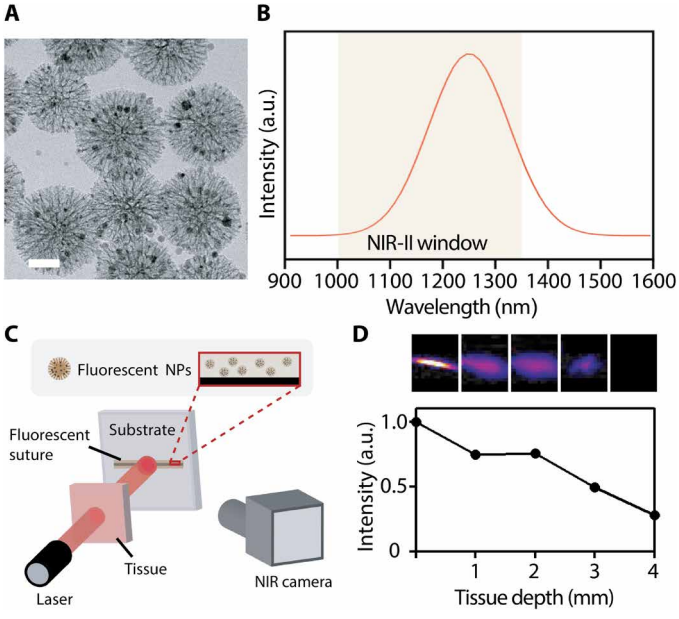

Fig. 5. Fluorescent suture for NIR bioimaging. (**A**) Representative transmission electron microscopy (TEM) image of $mSiO_2$@PbS/CdS-Fe_3O_4 fluorescent NPs. Scale bar, 50 nm. (**B**) Fluorescent emission spectrum of $mSiO_2$@PbS/CdS-Fe_3O_4 in the NIR-II window. a.u., arbitrary units. (**C**) Schematic of the ex vivo experimental setup to characterize the photoluminescence penetration of fluorescent NP–loaded TGS suture behind porcine tissue. (**D**) Representative fluorescence images (top) and normalized intensity (bottom) of the TGS sutures under tissues of varying thickness.

In vivo wound closure

To demonstrate the use of TGS sutures for wound closure, we further evaluated the wound healing of dorsal full-thickness skin incisions closed by pristine or TGS sutures in a rat model (Fig. 6L and fig. S14). The wounds were first assessed macroscopically on day 7, demonstrating good wound closure capability of both sutures, while no infection was observed (fig. S14). As expected, hydrogels on TGS sutures were dehydrated because of their exposure to the ambient environments. However, the hydrated hydrogel sheath was well preserved beneath the wound bed (fig. S14), indicating reliable suture-gel integrity during the mechanically demanding suturing and knotting process and the 1-week wound healing period. No loss or fragmentation of the gel sheath was observed during suturing and after placement. The potential dehydration of the hydrogel sheath for topical applications could be mitigated by applying a commercialized thin elastomer adhesive film (Tegaderm; 3 M) above the wound bed if needed (*41*). Histological assessment by a blinded pathologist confirmed that all the incisional wounds were healed by primary intention with minimum inflammation and fibrosis (Fig. 6, M and N).

DISCUSSION

Sutures are among the simplest and most widely used devices in clinical medicine. Despite recent efforts to make bioactive sutures, clinically used sutures remain largely passive, mechanical devices. The obstacles toward translation, in addition to the regulatory issue, include the lack of robust modification approaches and the limited functionality so far being integrated into the sutures. To overcome these issues, we first designed and constructed the TGS on various commercially available sutures and then engineered multifunctionality of the suture by exploiting salient attributes of hydrogel sheath such as softness, lubrication, antifouling, and transparency.

By rationally designing the anchoring and toughening networks of the TGS, we achieved an extremely tough suture-sheath interface as manifested by the experimentally measured adhesion energy beyond 2000 J m^{-2}. Such an interface managed to sustain the high mechanical loading during suturing and knotting. To put this value under context, the adhesion energy based on surface absorption and single-network hydrogels in the previously reported systems is below 100 J m^{-2} (*29*). To our knowledge, it is among the toughest interface achieved with hydrogels and the first reported tough adhesion between hydrogel and fiber-based materials.

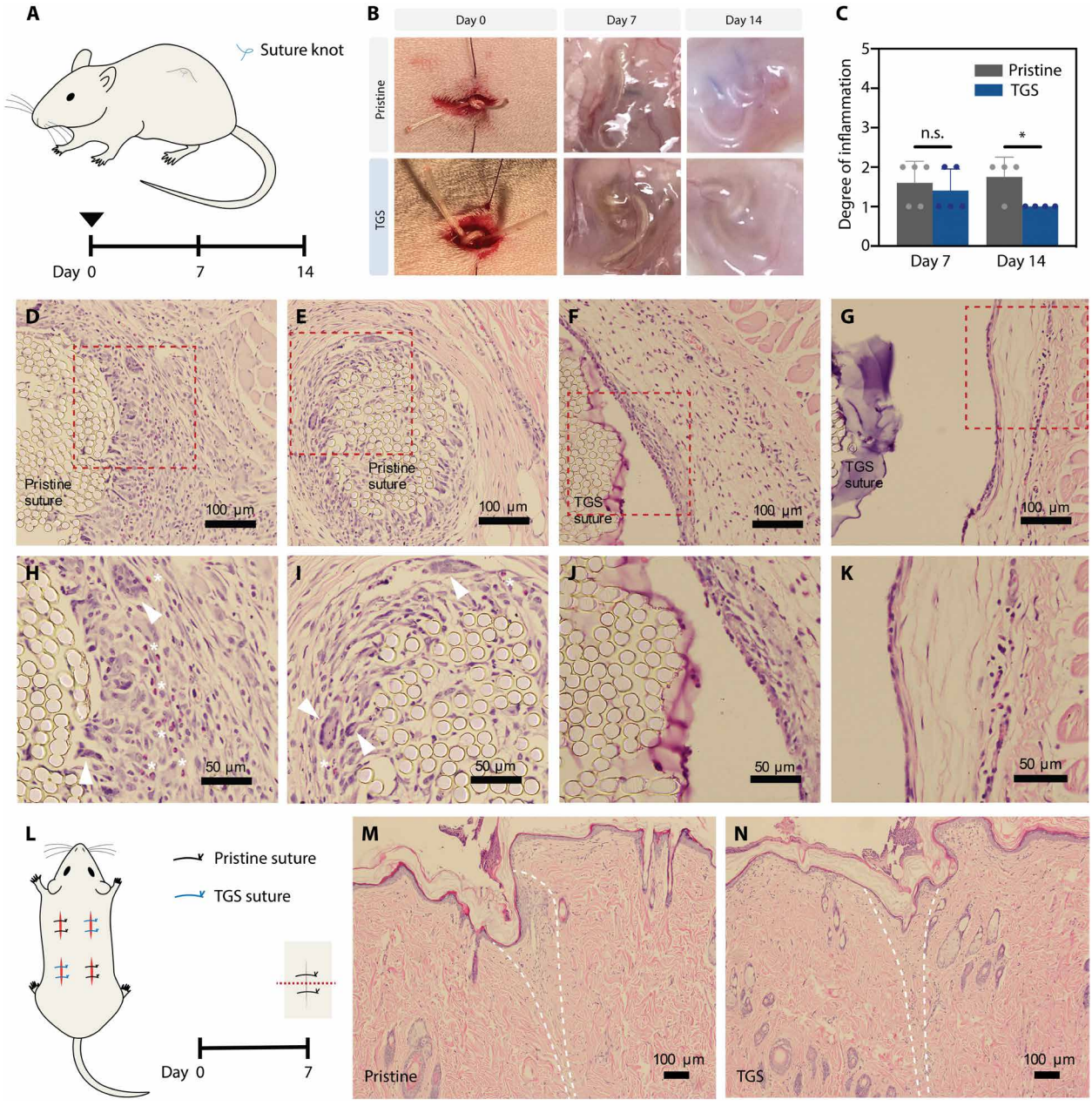

Fig. 6. In vivo biocompatibility and wound closure of pristine and TGS sutures. (**A**) Schematic illustration of the subcutaneous implantation of suture knots. The biocompatibility was assessed on days 7 and 14. (**B**) View of the suture knots implantation process and macroscopic inspection of the encapsulated suture knots on days 7 and 14. Photo credit: Zhenwei Ma and Qiman Gao, McGill University. (**C**) Degree of inflammation of implanted pristine and TGS sutures evaluated blindly by an experienced pathologist (0, normal; 1, very mild;, 2, mild; 3, moderate; 4, severe; 5, very severe). Statistical significance and *P* values are determined by two-sided Student's *t* test. "*" indicates $P < 0.5$; "n.s." indicates not significant. (**D** to **K**) Representative histology images stained with hematoxylin and eosin (H&E) of suture knot implanted for 7 days [pristine (D and H); TGS (F and J)] and 14 days [pristine (E and I); TGS (G and K)]. (H) to (K) are histological images of higher magnification of regions interest (rectangle with dashed red lines) from (D) to (G). White arrowheads indicate foreign body giant cells; star symbols indicate proinflammatory eosinophils. (**L**) Schematic illustration of incision wounds closed with pristine and TGS sutures as well as sections taken for histology (dotted red line) on day 7. (**M** and **N**) Representative histological images stained with H&E showing comparable wound healing outcome using pristine (M) and TGS (N) sutures, assessed blindly by an experienced pathologist ($n = 6$). Dashed white lines indicate wound edges.

Distinctive properties of the surgical suture can emerge with the robustly integrated TGS, which were proven to mitigate mechanical mismatch and irritation of sutures when interfacing with soft tissues. This is manifested in our in vivo implantation studies of TGS sutures, suggesting minimal inflammation reactions, while pristine sutures elicit more severe foreign body response. Because of the soft hydrated nature of hydrogels, the TGS provided a soft and lubricant surface, which decreased the surface stiffness and drag/friction coefficients by a factor of 10^4 and 3, respectively, without altering the tensile strength of the suture. Moreover, the hydrated surface of

TGS is inherently antifouling, evidenced by lowering the bacteria adhesion for both Gram-positive (*S. aureus*) and Gram-negative (*P. aeruginosa*) bacteria.

In addition, the TGS exhibited substantial attributes such as optical transparency and permeability to support the proper function of optical functional materials. In this work, it was exemplified with the pH-sensing microparticles and the fluorescent NPs for pH monitoring and NIR bioimaging, respectively. In both cases, the TGS effectively retained the payloads because of the small pore sizes. For pH sensing, the TGS is optically transparent and fully permeable to ionic species presented in the wound bed. For NIR bioimaging, both the excitation laser and the emission light from the fluorescent NPs can transmit through the hydrogel sheath without decay.

We further demonstrated the drug delivery capacity of the TGS to improve the therapeutic function of surgical sutures for advanced wound management. Our results showed that the TGS can encapsulate and release small-molecule antimicrobial compounds and protein model drugs to the wound site for infection prevention and tissue repair. The hydrogel sheath is expected to be compatible with other bioactive agents such as growth factors and cytokines owing to its hydrophilic nature. The drug loading capacity can be tuned by varying the drug concentration or the thickness of the hydrogel sheath, and the drug release kinetics can be modulated by engineering controlled release mechanisms of the hydrogel (*42*). These features make our strategy advantageous over the conventional dip-coating approach, which is limited by low loading capacity and burst release of drugs due to the lack of polymeric network to slow down the release (*15*). Smart drug delivery features could be further engineered within the TGS to locally enable triggered or stimuli-responsive drug release to the injured sites in a sustained manner to accelerate the wound healing process. By integrating bioactive reagents specific for certain application scenarios and individual patients, our method could potentially allow one to tailor surgical sutures for personalized therapies (*43*), while the tunable biophysical and biochemical niche could be further leveraged for cell encapsulation and delivery for advanced cell therapy (*44*).

TGS sutures are expected to be particularly beneficial for rejoining and reattaching mechanically active musculoskeletal tissues such as tendon. Compared with native tendon tissues, TGS sutures demonstrated much higher tensile strength yet lowered stretchability. Thus, biomimetic approach could be further developed to optimize TGS sutures with similar mechanical properties and nonlinear stress strain behaviors with native tendon tissues, providing adequate mechanical support for tendon rejoining, mitigating stress concentrations caused by traditional sutures, and applying appropriate biophysical cues to potentially accelerate tendon regeneration.

The current low-throughput production of TGS sutures limits their bench-to-bedside translational potentials. This could be resolved by adopting the industrialized dip-coating approaches, as indicated in our proof-of-concept demonstrations (fig. S15), although the rheological properties and polymerization conditions of the precursor solutions require further optimization.

A variety of hydrogels and suture materials are amenable to the design of TGS for robust surface functionalization. In particular, both mono- and multifilament sutures of varying diameters were successfully engineered to bond with the TGS. This strategy is auspicious for other fiber-based devices, including fibers, yarns, three-dimensional (3D)–printed scaffolds, guidewires, and continuum robots (*45*, *46*). As a demonstration, a 3D-printed polylactic acid fiber mesh was integrated with tough gel using the strategy developed in this work as a fiber-reinforced tough aortic patch (fig. S16). By leveraging our surface functionalization strategy, a bottom-up approach could be adopted to design more complex functional hybrid structures for 2D smart textiles and 3D scaffolds for materials and biomedical engineering. Biodegradation properties could be introduced by designing TGS containing (triggerable) degradable cross-linkers (e.g., disulfide bond and matrix metalloproteinase) (*47*, *48*). The broad applicability of the strategy reported here should ultimately provide a versatile basis to design and functionalize fiber-based devices that leverage new hydrogels and functional materials to evolve toward a desired form and function for different applications.

In summary, we reported a bioinspired design and method to robustly integrate clinically used surgical sutures, tough hydrogels, and various functional materials. Strong adhesion was realized at the suture-sheath interface and substantiated with extensive experimental characterization and computational simulation. A family of TGS sutures were developed, which achieved superior biomechanical performance and multiple functionality. The TGS sutures exhibited tissue-like stiffness, low drag, and friction on the contacting tissue without compromising the tensile strength. The suture sheath provided a versatile platform to merge the suture with functional materials for the diagnostic, monitoring, and therapeutic functions. Applications of anti-infection, wound bed pH sensing, drug delivery, and NIR bioimaging were demonstrated within a single platform for advanced wound management. The facile generation of TGS suggested an extensive design flexibility for other fiber-based devices such as textiles and fabrics. This platform is an important step toward integration of hydrogel technologies, functional materials, and fiber-based devices to develop next-generation multifunctional materials. This work would open new avenues for the development of surgical tools, wearable and implantable devices, soft robotics, and fiber and textile materials.

MATERIALS AND METHODS

Fabrication of TGS sutures

The essential fabrication procedure is illustrated with polyglactin 910 sutures (Coated VICRL, 2-0, Ethicon). First, the suture was surface-treated with 1 M NaOH solution for 2 min and then rinsed with deionized (DI) water before air drying. The surface-activated suture was then inserted into a glass capillary tube (World Precision Instrument, TW120-6) as a microreactor, which defines the thickness of tough sheath and provides a closed environment for polymerization. Chitosan of high deacetylation degree (>95%; Lyphar Biotech) was dissolved at 2% concentration in 0.2 M acetic acid solution. EDC and NHS (Sigma-Aldrich) were vortexed and mixed with the chitosan solution both at a final concentration of 40 mg/ml. The mixture was then injected into the capillary tube through a 25-gauge needle (Sigma-Aldrich) to prime the suture surface for 10 min. The prepolymer solutions for alginate-PAAm hydrogels, containing 2% sodium alginate (high molecular weight, I1G, KIMICA Corporation), 16% acrylamide (Sigma-Aldrich), 0.01% *N*,*N*′-methylenebis (acrylamide) (MBAA; Sigma-Aldrich), 0.03% ammonium persulfate (APS; Sigma-Aldrich), and 0.46% tetramethylethylenediamine (TEMED; Sigma-Aldrich) and inclusions (if any; e.g., drugs and microparticles) were syringe-mixed, then injected

into the capillary tube, and replaced the chitosan solution. Two customized plugs with centered through-holes were 3D-printed with an Autodesk Ember desktop 3D printer and capped at the two ends of the tube to enable the coaxial structure of the hybrid suture. After an overnight reaction, the sheathed suture was retrieved from the tube and later immersed in 0.1 M $CaCl_2$ solution for 5 min to further cross-link the alginate before usage.

Scanning electron microscopy

The pristine or TGS sutures were frozen at −80°C and subsequently lyophilized for 24 hours with a freeze dryer (Labconco Freezone). The freeze-dried sutures were coated with 4-nm platinum using a high-resolution sputter coater (ACE600, Leica) to increase the surface conductivity. A scanning electron microscope (FEI Quanta 450 environmental) was used to image the specimens at 5 kV and 10 mA under various magnifications.

Mechanical characterization

The pristine or TGS sutures were pulled uniaxially using an Instron machine (model 5965; load cell: 1 kN) at a displacement rate of 0.5 mm/s, while the force and displacement were recorded. The tensile strength was determined from the peak stress at failure. The sample length was 20 mm for all the tests.

Atomic force microscope

An atomic force microscope (JPK NanoWizard 3, Berlin, Germany) was used to conduct microindentation tests to measure the microscale Young's modulus of suture surface. Rectangular silicon cantilevers with 25-μm in-diameter spherical beads attached as probes were used (Novascan, IA, USA). Cantilevers with a nominal spring constant of 0.6 N/m were used for testing the sheathed sutures and of 2 N/m for the pristine sutures. The spring constants of the cantilevers were determined with a thermal noise method before the experiments. Indentations were conducted at 20 different locations for each sample. The Hertzian contact model was used to calculate the Young's moduli (*49*).

Specimen fabrication for adhesion testing

Sutures with relatively thicker sheath were fabricated for characterizing the adhesion energy between the suture and the tough hydrogel sheath. Briefly, for alg-PAAm–sheathed polyglactin 910 suture (Coated VICRL, 2, Ethicon), sutures were treated with 1 M NaOH solution with various durations (2, 5, and 10 min) or without any treatment. It was then primed with 2% chitosan solution containing EDC/NHS (40 mg/ml) for 10 min and then placed inside a customized acrylic mold of designed dimensions (width, 30 mm; length, 50 mm; height, 3 mm), with one end sticking out of the mold. Prepolymer solution was then applied into the mold and sealed with another layer of acrylic sheet, and the hybrid was allowed for full gelation overnight. The prepolymers for different hydrogel cuboids are as follows: 2% sodium alginate, 16% acrylamide, 0.01% MBAA, 0.03% APS, 0.46% TEMED, and 20 mM $CaSO_4$ for alginate-PAAm hydrogels; 2% alginate solution containing 40 mM $CaSO_4$ for alginate hydrogels; 16% acrylamide, 0.01% MBAA, 0.03% APS, and 0.46% TEMED for PAAm hydrogels; a solution containing 2.5% chitosan and 35.5% acrylamide was mixed with 21.6 μl of 2% MBAA, 135.6 μl of 0.27 M APS, and 4.02 ml of chitosan-gelling agent (consisting of 0.1 M Na_2HPO_4, 0.1 M NaH_2PO_4, and 0.306 M $NaHCO_3$) for PAAm-chitosan hydrogel. The other sheathed sutures were based on alginate-PAAm hydrogels, while nylon suture (3-0, Ethilon, Ethicon) was treated with 1 M HCl for 1 hour, and plain gut (6-0, Ethicon) was used as received, before surface priming and in situ gelation as previously described.

Adhesion energy characterization

The adhesion energy between the suture and the hydrogel sheath was characterized using a customized pull-out test with an Instron machine. Two acrylic sheets were glued onto two opposing sides of a hydrogel cuboid as rigid constraints. To apply a full constraint on the hydrogel sheaths, the backing of the suture-gel hybrid is fixed on to the bottom grip of the Instron machine, while the exposed suture end was fixed on to the upper grip. The suture was pulled out unidirectionally at a displacement rate of 0.5 mm/s, while the force F and the displacement δ were recorded. The critical energy release rate, i.e., adhesion energy, was calculated with Eq. 1.

Finite element modeling

The simulation was carried out with ABAQUS (Version 2020, SIMULIA). The axisymmetric assumption was made to reduce the problem to 2D to save the computation time (fig. S6, A to C). The top end of the suture is subjected to a constant loading rate $\dot{\delta} = 0.01$ mm/s, while the right edge of the hydrogel sheath is fixed in all degrees of freedom (fig. S6C). The computational study provides a qualitative trend insensitive to the exact geometric parameters of the hydrogel sheath and the boundary conditions.

The hydrogel sheath was modeled as an incompressible Ogden hyperelastic material with Mullins effect to account for the mechanical dissipation. The strain energy density for the incompressible Ogden model is given by

$$U = \frac{2\mu}{\alpha^2}(\lambda_1^\alpha + \lambda_2^\alpha + \lambda_3^\alpha - 3)$$

where U is the strain energy density, μ is the shear modulus, α is the fitting coefficient, and λ_i is the ith principle stretch (i = 1, 2, and 3). The nominal stress S for a pure-shear test is then given by

$$S = \frac{2\mu}{\alpha}\left(\lambda^{\alpha-1} - \lambda^{-(\alpha+1)}\right) \quad (2)$$

The Ogden model coefficients were obtained by fitting Eq. 2 to the loading paths in the pure-shear test results of the alg-PAAm hydrogel (fig. S7F). The shear modulus μ and α were fitted to be 34.9 kPa and 1.60, respectively. The model for the Mullin's effect is given by

$$\begin{aligned} W &= \eta\,\widehat{W} + \phi(\eta) \\ \phi(\eta) &= \int_1^\eta \left[(m + \beta W^m)\,\mathrm{erf}^{-1}(r(1-\eta)) - W^m\right] d\eta \\ h &= \frac{1}{r}\left[\mathrm{erf}\left(\frac{U}{m+\beta U}\right) - \frac{m+\beta U}{\sqrt{\pi}\,U}\left[1 - \exp\left[-\left(\frac{U}{m+\beta U}\right)^2\right]\right]\right] \end{aligned} \quad (3)$$

where η is the damage variable (η = 1 and η = 0 represents the material in its virgin and the completely damaged state, respectively), $\widehat{W}$ is the strain energy density without energy dissipation, W^m is the maximum strain energy density before unloading, φ(η) is the damage function, and erf is the error function. r = 1.33, m = 27.35, and β = 0.2818 are fitting coefficients and were obtained by fitting

Eq. 3 to the hysteresis ratios h against the external work U, where h is interpreted as the ratio of the loop area to the area under the loading paths (fig. S7F). The suture was modeled as linear elastic with the elastic modulus of 300 GPa, measured from the slope of the stress-strain curve of the pristine suture in (Fig. 3A), and the Poisson's ratio of 0.3. The interface was characterized as a layer of cohesive elements, modeled with a triangular traction-separation law (fig. S6G). δ_{max} andS_{max} are the prescribed maximum displacement and strength, respectively, and the area under the curve is the intrinsic adhesion toughness Γ_0. The damage initiation is governed by the quadratic nominal stress criterion

$$\left(\frac{t_n}{S_{max}}\right)^2 + \left(\frac{t_s}{S_{max}}\right)^2 = 1 \tag{4}$$

where t_n and t_s are the stresses in the directions normal and tangential to the joint interface, respectively. Mesh convergence tests were carried out to determine the appropriate number of elements applied in each model. In the loading regime for the case with r_g/r_s = 1, the results obtained with different mesh sizes were indistinguishable; in the debonding regime, the results with the smallest mesh sizes of 0.075 and 0.05 mm showed a good agreement, indicating that the results were insensitive to the mesh size adopted in the current simulation (0.05 mm) (fig. S6H).

Derivation of energy release rate *G*

The schematic of the suture with hydrogel sheath simulated in FEM was shown in fig. S7. The radius of 2D axisymmetric cross section in the $r - z$ plane of suture and the thickness of the gel are r_s and r_g, respectively, and $r_{tot} = r_g + r_s$. The two parts are adhered together with a joint length L.

Upon the pulling of the suture while the outer surface of the hydrogel sheath is fixed, the interface of the joint sustains the shear stress

$$\tau = \frac{F}{(2\pi r_s L)} \tag{5}$$

presumably, the shear stress is uniform over the joined region, and the joint parts hydrogel and the suture are under simple shear and tensile loadings with uniform shear and normal strains γ_g and γ_s. The corresponding shear and normal stresses in the hydrogel and the suture are $\tau(\gamma_g) = F/(2\pi r_s L)$ and $\tau(\gamma_s) = F/(\pi r_s^2)$, respectively. The integration of the stress over the associated strain defines the strain energy density stored in the materials

$$U_i = \int \tau(\gamma_i)\, d\gamma_i \tag{6}$$

where the subscription i can be g or s, standing for the hydrogel or the suture, respectively. In a quasi-static loading process, the work done by the pulling force on the suture and the hydrogel at a given applied displacement δ is completely converted to the elastic energy stored in the materials. Thus, the strain energy densities in the gel and the suture also have the form

$$\begin{aligned} U_g &= \frac{\int F(\delta_g)\, d\delta_g}{\pi(r_{tot}^2 - r_s^2) L} \\ U_s &= \frac{\int F(\delta_s)\, d\delta_s}{\pi(r_s^2) L} \end{aligned} \tag{7}$$

where δ_g and δ_s are the distance that the 2D gel and suture sections are deformed along the pulling direction, and $\delta = \delta_g + \delta_s$. The shear strain in the 2D hydrogel sheath γ_g and the suture γ_s can be obtained by substituting the stress expressions into Eq. 6 and then equating Eq. 7

$$\gamma_s = \frac{\delta_s}{L}, \gamma_g = \frac{\delta_g}{\frac{r_g^2}{2r_s} + r_g} \tag{8}$$

The total potential energy of the system, consisting of the elastic energy stored in the materials and the potential energy by the pulling force, is given by

$$\Pi = U_s L\pi r_s^2 + U_g L\pi(r_{tot}^2 - r_s^2) - F(\delta_s + \delta_g) \tag{9}$$

During a quasi-static crack growth dc, the joint length reduces by the same amount. Thus, the energy release rate is determined by $-\partial\Pi/(2\pi r_s \partial c)$, or equivalently by

$$G = \frac{\partial \Pi}{2\pi r_s \partial L} \tag{10}$$

Combining Eqs. 8, 9, and 10 and leveraging the critical condition for the crack propagation $G = \Gamma$ lead to

$$\begin{aligned} \Gamma &= \left[\frac{\partial U_s}{\partial \tau}\frac{\partial \tau}{\partial L} L\pi r_s^2 + \frac{\partial U_g}{\partial \tau}\frac{\partial \tau}{\partial L} L\pi\left(r_{tot}^2 - r_s^2\right)\right]\frac{1}{2\pi r_s} + \left[U_s \pi r_s^2 + U_g \pi\left(r_{tot}^2 - r_s^2\right)\right]\frac{1}{2\pi r_s} \\ &\quad - \left[F\frac{\partial \delta_s}{\partial \gamma_s}\frac{\partial \gamma_s}{\partial \tau}\frac{\partial_r}{\partial L} + F\frac{\partial \delta_g}{\partial \gamma_g}\frac{\partial \gamma_g}{\partial \tau}\frac{\partial \tau}{\partial L}\right]\frac{1}{2\pi r_s} \\ &= \frac{1}{2\pi r_s}\left[U_s \pi r_s^2 + U_g \pi\left(r_{tot}^2 - r_s^2\right)\right] \end{aligned} \tag{11}$$

Because the elastic modulus of the suture is ~100,000 times higher than that of the hydrogel sheath while their radii are of the same order of magnitude, the latter bears most of the strain energy. Thus, it is safe to remove the term with U_s, and the expression can be further reduced to the Eq. 1.

Shear stress distribution analysis from FEM

The nonmonotonic correlation between Γ/Γ_0 and r_g/r_s was shown in Fig. 2D, i.e., it increases in the range of $2 < r_g/r_s < 4$ and decreases in the range of $r_g/r_s \leq 2$ with decreasing r_g/r_s. To understand the phenomenon, the magnitude of the normalized shear stress $|S_{shear}/S_{max}|$ along the joint interface as a function of the applied displacement $\delta$and distance z (fig. S7, A to C) was examined. The results for r_g/r_s = 1 and 4 are shown in fig. S7 (D and E), respectively. In both cases, $|S_{shear}/S_{max}|$ is uniform along the interface and increases monotonically at small δ values. As δ increases to larger values, $|S_{shear}/S_{max}|$ for r_g/r_s = 1 increases to 1 and then rapidly decreases to 0, indicating that the joint interface debonds simultaneously after reaching the prescribed maximum strength. On the other hand, when r_g/r_s = 4, $|S_{shear}/S_{max}|$ in a small region near the top reaches the prescribed strength first and then rapidly decreases to 0, hindering the uncracked region from reaching the maximum strength. Consequently, the energy dissipation is confined in the small region, leading to smaller Γ/Γ_0 with higher r_g/r_s.

Drag coefficient characterization

A customized drag coefficient characterization method, recapitulating the dragging experienced at tissue-suture interface during the suturing process, was developed. We termed it drag coefficient to differentiate it from the standard friction coefficient characterization. The tissues (porcine heart, liver, or heart) were cut into similar sizes and kept in phosphate-buffered saline (PBS) before testing. A 100 g of weight was attached to the tissue. Suture was then passed through the tissue. One end of the suture was affixed to a laboratory stand, while the other end clamped to the load cell. The position of the stand remained constant for all the samples tested. The Instron was set to cycle five times over a 50-mm distance at a speed of 3 mm/s. To interpret the data, the drag coefficient μ_d was calculated using the following formula

$$\mu_d = (F_A - F_D)/(F_A + F_D) \quad (12)$$

where F_A denotes the average maximum (ascending crosshead) force and F_D denotes the average minimum (descending crosshead) force.

Sutured cartilage-PDMS friction coefficient characterization

A custom-built scaffold made of aluminum T-slots was assembled for the friction coefficient testing. Porcine cartilage was purchased from local butcher shop. A PDMS sheet was fixed to an aluminum plate, which could slide freely along a trail fixed onto the bottom surface. One end of the plate was connected to an inextensible string attached to the load cell through a pulley system. Two fixtures connected with an aluminum beam were inserted into the trail of the two standing frames of the scaffold, which could slide freely vertically. The top side of the cartilage was glued onto the beam, while the intact bottom side contacted with the PDMS sheet. During the test, the fixtures/beam and applied weight together induced a compressive stress to make sure of the intimate contact between the cartilage and the PDMS sheet so that the friction coefficient could be measured. The PDMS sheet was then subjected to a displacement with a constant loading rate (0.5 mm/s), and the force was recorded by the load cell. The friction coefficient μ_f was determined using the following equation

$$\mu_f = F_p/F_c \quad (13)$$

where F_p denotes the averaged plateau force, and F_c denotes the compressive force applied. The sutured cartilage was prepared by applying continuous stitches using pristine polyglactin 910 suture or alg-PAAm hydrogel–sheathed polyglactin 910 suture onto the bottom surface of the cartilage. The samples were tested as previously described, and the friction coefficient was calculated accordingly using Eq. 13.

Antibacterial study

The bacterial strains used were the Gram-positive bacteria *S. aureus* (American Type Culture Collection 25923) and Gram-negative *P. aeruginosa* (PAO1). Bacterial cultures were refreshed on nutrient agar from −80°C stocks. To grow bacterial suspensions, single colonies were transferred to Luria-Bertani broth and incubated overnight at 37°C and 220 rpm. Bacterial cells were harvested at logarithmic growth phase and centrifuged at 4000*g* for 10 min (Heraeus Multifuge X3R, Thermo Fisher Scientific, USA). The cells were resuspended in PBS, and the optical density of the suspension at 600 nm was adjusted to 0.3 using an ultraviolet (UV)–visible spectrophotometer (Biomate 3S, Thermo Fisher Scientific, USA). Polyglactin 910 suture was used without any modification as pristine suture; alg-PAAm–sheathed polyglactin 910 suture was used as the TGS suture; TGS suture with loaded BZK was prepared by immersing TGS suture in 10% BZK solution overnight and subsequently washed three times in PBS solution before testing. Each suture sample was immersed in 1-ml bacterial suspension and incubated for 1 hour. The suture was then removed and rinsed with PBS to remove loosely attached cells. Before imaging each sample, bacteria were stained using the Live/Dead BacLight Viability Kit (Molecular Probes Inc., USA) using a mixture of SYTO9 and propidium iodide. SYTO9 can cross the membrane of all bacteria in a population, staining them green, whereas propidium iodide only permeates the cells with compromised membranes (referred to as dead), staining them red. The samples were imaged using a confocal laser scanning microscope (LSM 710, Zeiss, Germany). Multiple images were taken from each sample, and the experiments were repeated three times. Viability was calculated as the percentage of live bacteria over total number of bacteria in each image.

pH monitoring

The pH sensing beads were prepared by doping mesoporous resin beads with a pH-responsive dye. Briefly, Brilliant Yellow dye (TCI, Tokyo, Japan) was dissolved in an ethanol solution (20%) at 4.5 mg/ml. Dowex 1 × 4 chloride form (Sigma-Aldrich) was thoroughly washed with DI water and ethanol and then added to the dye solution. The supernatant was washed several times until a clear solution was obtained. The pH-sensing beads were collected and mixed with alg-PAAm prepolymer solution containing Iragure 2959 (Sigma-Aldrich) as a photoinitiator, because APS could be absorbed by the resin. Both bulk hydrogel and suture-hydrogel hybrid were prepared under UV light (365 nm) for 1 hour. The hydrogel was immersed in solution of different pH for 5 min. Photo was taken and converted to 8-bit images, and the gray scale of each sample was analyzed using ImageJ.

Drug release study

FITC-albumin (A9771, Sigma-Aldrich) was dissolved in DI water at 30 mg/ml. Pristine suture was first treated with 1 M NaOH solution for 2 min, rinsed with DI water, and air-dried to increase the hydrophilicity of the suture surface. The surface-activated suture was then immersed in FITC-albumin solution overnight. Suture-gel hybrid was fabricated using prepolymer solution made with FITC-albumin solution and left overnight before retrieved from the device. Both pristine sutures and suture-gel hybrids were cut into 1-cm-long threads, subsequently transferred to a 12-well plate with 0.5-ml DI water in each plate, and incubated in the dark at 37°C. At each time point, a 50-μl aliquot of the solution was collected, and the fluorescence intensity was measured using a plate reader. A standard curve was obtained by measuring the intensity of different solution with different FITC-albumin concentration and used as a reference to calculate the cumulative release profile for each sample.

Synthesis and characterization of fluorescent NP–loaded TGS sutures

The fluorescence NPs, $mSiO_2$@PbS/CdS-Fe_3O_4, were synthesized using a modified protocol reported previously (*39*). The

morphology of as-prepared NPs was investigated by transmission electron microscopy (TEM; JEOL 2100F) at 200 kV equipped with a charge-coupled device camera. Energy-dispersive x-ray spectroscopy was taken on specific areas during TEM measurements. Fluorescent emission spectra were acquired on the Fluorolog-3 System (Horiba Jobin Yvon) using an excitation wavelength of 600 nm. Fluorescent NP–loaded TGS suture was obtained by mixing the fluorescent NPs into alg-PAAm prepolymer solution before in situ gelation.

NIR bioimaging

To demonstrate deep-tissue penetration property of fluorescent NP–loaded TGS suture, a homemade setup was designed to take NIR images ex vivo, as shown in Fig. 4D. Briefly, fluorescent NP–loaded TGS suture with a length of 3 cm was fixed on a holder that was covered with pieces of porcine tissue of different thickness (or without). An 806-nm laser with a power density of 10 W/cm^2 was used to excite the NIR suture through the porcine tissue. Meanwhile, NIR images were recorded by a Xeva-1.7 infrared camera (Xenics Corp, Belgium) equipped with an 830-nm long-pass optical filter to block the light below 830 nm and the scattered excitation light of the 806-nm laser.

In vitro biocompatibility assay

To assess the cell compatibility of the TGS sutures, human vocal fold fibroblasts were cultured in 24-well plates at 10^6 ml^{-1} cell density in conditioned medium containing Dulbecco's modified Eagle's medium (Life Technologies, ON) and supplemented with 10% fetal bovine serum, 1% penicillin/streptomycin, and 1% minimum essential medium nonessential amino acids, along with 1-cm-long TGS suture or no suture as control. Cell viability was assessed using the LIVE/DEAD Viability Kit (Invitrogen, L3224) after 48-hour culture and was imaged using a confocal laser scanning microscope (LSM 710, Zeiss, Germany). Live cells were shown in green fluorescence, and dead cells were shown in red.

In vivo biocompatibility and wound healing

All animal surgical procedures were reviewed and approved by the Facility Animal Care Committees at McGill University and the Research Institute of McGill University Health Centre. Female Sprague Dawley rats (200 to 300 g, Charles River Laboratories) were used for all in vivo studies. All hydrogel precursor solutions prepared for TGS suture fabrication were sterilized with 0.2-μm filters. Pristine sutures (2-0 and 5-0, Coated VICRYL, Ethicon) were used as received. For in vivo biocompatibility assays, a small incision (typically 1 cm) was made through the dorsal subcutaneous tissue of rats, and a pair of scissors was used to create a small pocket. TGS or pristine suture (1.5 cm long) was made into a knot and implanted into the subcutaneous pocket (n = 6). The incisions were then closed with the 5-0 VICRYL sutures. At 7 and 14 days, animals were euthanized, and the implanted sutures and surrounding tissues were excised and fixed in 4% formalin for 24 hours for histological analyses. To examine the effect of TGS and pristine sutures on wound closure and healing, four 1.5-cm-long full-thickness skin incision without tissue loss were created with a scalpel on the lateral dorsum of each rat. The wounds were closed using either TGS or pristine sutures (n = 6) with an interrupted pattern. Rats were euthanized after 7 days. Tissues with regions of interest were excised and fixed in 4% formalin for 24 hours for histological analyses.

Histological processing

Fixed tissue samples were placed into 70% ethanol and submitted for histological processing and hematoxylin and eosin staining at the Centre for Bone and Periodontal Research at McGill University. Z.-H.G. is the pathologist-in-chief at McGill University Health Centre and examined all histological sections.

Statistical analysis

Comparative data analysis has been performed on friction coefficient characterization [(sutured) cartilage-PDMS] and bacteria adhesion on pristine or TGS suture with or without BZK inclusion using a two-tailed, one-way analysis of variance (ANOVA) with a Holm-Sidak post hoc pairwise comparison test. All statistical analyses were conducted in SigmaStat 3.5 (Systat Software Inc., San Jose, CA, USA).

SUPPLEMENTARY MATERIALS

Supplementary material for this article is available at http://advances.sciencemag.org/cgi/content/full/7/15/eabc3012/DC1

REFERENCES AND NOTES

1. J. V. Clough, J. Alexander-Williams, Surgical and economic advantages of polyglycolic-acid suture material in skin closure. *Lancet* **305**, 194–195 (1975).
2. R. E. Abhari, J. A. Martins, H. L. Morris, P.-A. Mouthuy, A. Carr, Synthetic sutures: Clinical evaluation and future developments. *J. Biomater. Appl.* **32**, 410–421 (2017).
3. J. Li, A. D. Celiz, J. Yang, Q. Yang, I. Wamala, W. Whyte, B. R. Seo, N. V. Vasilyev, J. J. Vlassak, Z. Suo, D. J. Mooney, Tough adhesives for diverse wet surfaces. *Science* **357**, 378–381 (2017).
4. H. Yuk, C. E. Varela, C. S. Nabzdyk, X. Mao, R. F. Padera, E. T. Roche, X. Zhao, Dry double-sided tape for adhesion of wet tissues and devices. *Nature* **575**, 169–174 (2019).
5. J. Deng, H. Yuk, J. Wu, C. E. Varela, X. Chen, E. T. Roche, C. F. Guo, X. Zhao, Electrical bioadhesive interface for bioelectronics. *Nat. Mater.* **20**, 229–236 (2021).
6. X. Xu, X. Xia, K. Zhang, A. Rai, Z. Li, P. Zhao, K. Wei, L. Zou, B. Yang, W.-K. Wong, P. W.-Y. Chiu, L. Bian, Bioadhesive hydrogels demonstrating pH-independent and ultrafast gelation promote gastric ulcer healing in pigs. *Sci. Transl. Med.* **12**, eaba8014 (2020).
7. J. Chen, D. Wang, L.-H. Wang, W. Liu, A. Chiu, K. Shariati, Q. Liu, X. Wang, Z. Zhong, J. Webb, R. E. Schwartz, N. Bouklas, M. Ma, An adhesive hydrogel with "load-sharing" effect as tissue bandages for drug and cell delivery. *Adv. Mater.* **32**, 2001628 (2020).
8. D. E. Discher, D. J. Mooney, P. W. Zandstra, Growth factors, matrices, and forces combine and control stem cells. *Science* **324**, 1673–1677 (2009).
9. L. Van De Water, S. Varney, J. J. Tomasek, Mechanoregulation of the myofibroblast in wound contraction, scarring, and fibrosis: Opportunities for new therapeutic intervention. *Adv. Wound Care* **2**, 122–141 (2013).
10. E. B. Hunziker, A. Stähli, Surgical suturing of articular cartilage induces osteoarthritis-like changes. *Osteoarthritis. Cartilage* **16**, 1067–1073 (2008).
11. L. Shahinian Jr., S. I. Brown, Postoperative complications with protruding monofilament nylon sutures. *Am. J. Ophthalmol.* **83**, 546–548 (1977).
12. B. R. Freedman, D. J. Mooney, Biomaterials to mimic and heal connective tissues. *Adv. Mater.* **31**, 1806695 (2019).
13. C.-C. Chu, D. F. Williams, Effects of physical configuration and chemical structure of suture materials on bacterial adhesion: A possible link to wound infection. *Am. J. Surg.* **147**, 197–204 (1984).
14. Ethicon, Wound closure manual. Somerville, NJ: Johnson & Johnson; www.ethicon.com/.
15. M. Champeau, J.-M. Thomassin, T. Tassaing, C. Jérôme, Current manufacturing processes of drug-eluting sutures. *Expert Opin. Drug Deliv.* **14**, 1293–1303 (2017).
16. C. B. Weldon, J. H. Tsui, S. A. Shankarappa, V. T. Nguyen, M. Ma, D. G. Anderson, D. S. Kohane, Electrospun drug-eluting sutures for local anesthesia. *J. Control. Release* **161**, 903–909 (2012).
17. M. Akbari, A. Tamayol, V. Laforte, N. Annabi, A. H. Najafabadi, A. Khademhosseini, D. Juncker, Composite living fibers for creating tissue constructs using textile techniques. *Adv. Funct. Mater.* **24**, 4060–4067 (2014).
18. D. R. Ceratti, B. Louis, X. Paquez, M. Faustini, D. Grosso, A new dip coating method to obtain large-surface coatings with a minimum of solution. *Adv. Mater.* **27**, 4958–4962 (2015).
19. L. Wang, D. Chen, J. Sun, Layer-by-layer deposition of polymeric microgel films on surgical sutures for loading and release of ibuprofen. *Langmuir* **25**, 7990–7994 (2009).

20. J. S. Lee, Y. Lu, G. S. Baer, M. D. Markel, W. L. Murphy, Controllable protein delivery from coated surgical sutures. *J. Mater. Chem.* **20**, 8894–8903 (2010).
21. Y. Yong, M. Qiao, A. Chiu, S. Fuchs, Q. Liu, Y. Pardo, R. Worobo, Z. Liu, M. Ma, Conformal hydrogel coatings on catheters to reduce biofouling. *Langmuir* **35**, 1927–1934 (2019).
22. G. Parada, Y. Yu, W. Riley, S. Lojovich, D. Tshikudi, Q. Ling, Y. Zhang, J. Wang, L. Ling, Y. Yang, S. Nadkarni, C. Nabzdyk, X. Zhao, Ultrathin and robust hydrogel coatings on cardiovascular medical devices to mitigate thromboembolic and infectious complications. *Adv. Healthc. Mater.* **9**, 2001116 (2020).
23. S. Saxena, A. R. Ray, A. Kapil, G. Pavon-Djavid, D. Letourneur, B. Gupta, A. Meddahi-Pellé, Development of a new polypropylene-based suture: Plasma grafting, surface treatment, characterization, and biocompatibility studies. *Macromol. Biosci.* **11**, 373–382 (2011).
24. M. Champeau, J.-M. Thomassin, T. Tassaing, C. Jerome, Drug loading of sutures by supercritical CO_2 impregnation: Effect of polymer/drug interactions and thermal transitions. *Macromol. Mater. Eng.* **300**, 596–610 (2015).
25. J. Li, S. W. Linderman, C. Zhu, H. Liu, S. Thomopoulos, Y. Xia, Surgical sutures with porous sheaths for the sustained release of growth factors. *Adv. Mater.* **28**, 4620–4624 (2016).
26. J. Yang, R. Bai, Z. Suo, Topological adhesion of wet materials. *Adv. Mater.* **30**, 1800671 (2018).
27. W. Li, X. Liu, Z. Deng, Y. Chen, Q. Yu, W. Tang, T. L. Sun, Y. S. Zhang, K. Yue, Tough bonding, on-demand debonding, and facile rebonding between hydrogels and diverse metal surfaces. *Adv. Mater.* **31**, 1904732 (2019).
28. H. Yuk, T. Zhang, G. A. Parada, X. Liu, X. Zhao, Skin-inspired hydrogel–elastomer hybrids with robust interfaces and functional microstructures. *Nat. Commun.* **7**, 12028 (2016).
29. Y. Yu, H. Yuk, G. A. Parada, Y. Wu, X. Liu, C. S. Nabzdyk, K. Youcef-Toumi, J. Zang, X. Zhao, Multifunctional "hydrogel skins" on diverse polymers with arbitrary shapes. *Adv. Mater.* **31**, 1807101 (2019).
30. P. Kannus, Structure of the tendon connective tissue. *Scand. J. Med. Sci. Sports* **10**, 312–320 (2000).
31. J.-Y. Sun, X. Zhao, W. R. K. Illeperuma, O. Chaudhuri, K. H. Oh, D. J. Mooney, J. J. Vlassak, Z. Suo, Highly stretchable and tough hydrogels. *Nature* **489**, 133–136 (2012).
32. H. Yuk, T. Zhang, S. Lin, G. A. Parada, X. Zhao, Tough bonding of hydrogels to diverse non-porous surfaces. *Nat. Mater.* **15**, 190–196 (2016).
33. T. Zhang, S. Lin, H. Yuk, X. Zhao, Predicting fracture energies and crack-tip fields of soft tough materials. *Extreme Mech. Lett.* **4**, 1–8 (2015).
34. G. Zhang, T. Ren, X. Zeng, E. Van Der Heide, Influence of surgical suture properties on the tribological interactions with artificial skin by a capstan experiment approach. *Friction.* **5**, 87–98 (2017).
35. A. Valiei, M. Okshevsky, N. Lin, N. Tufenkji, Anodized aluminum with nanoholes impregnated with quaternary ammonium compounds can kill pathogenic bacteria within seconds of contact. *ACS Appl. Mater. Interfaces* **10**, 41207–41214 (2018).
36. L. A. Schneider, A. Korber, S. Grabbe, J. Dissemond, Influence of pH on wound-healing: A new perspective for wound-therapy? *Arch. Dermatol. Res.* **298**, 413–420 (2007).
37. A. Tamayol, M. Akbari, Y. Zilberman, M. Comotto, E. Lesha, L. Serex, S. Bagherifard, Y. Chen, G. Fu, S. K. Ameri, W. Ruan, E. L. Miller, M. R. Dokmeci, S. Sonkusale, A. Khademhosseini, Flexible pH-sensing hydrogel fibers for epidermal applications. *Adv. Healthc. Mater.* **5**, 711–719 (2016).
38. G. Hong, A. L. Antaris, H. Dai, Near-infrared fluorophores for biomedical imaging. *Nat. Biomed. Eng.* **1**, 0010 (2017).
39. F. Yang, A. Skripka, M. S. Tabatabaei, S. H. Hong, F. Ren, Y. Huang, J. K. Oh, S. Martel, X. Liu, F. Vetrone, D. Ma, Magnetic photoluminescent nanoplatform built from large-pore mesoporous silica. *Chem. Mater.* **31**, 3201–3210 (2019).
40. Z. Hu, C. Fang, B. Li, Z. Zhang, C. Cao, M. Cai, S. Su, X. Sun, X. Shi, C. Li, T. Zhou, Y. Zhang, C. Chi, P. He, X. Xia, Y. Chen, S. S. Gambhir, Z. Cheng, J. Tian, First-in-human liver-tumour surgery guided by multispectral fluorescence imaging in the visible and near-infrared-I/II windows. *Nat. Biomed. Eng.* **4**, 259–271 (2020).
41. S. O. Blacklow, J. Li, B. R. Freedman, M. Zeidi, C. Chen, D. J. Mooney, Bioinspired mechanically active adhesive dressings to accelerate wound closure. *Sci. Adv.* **5**, eaaw3963 (2019).
42. J. Li, D. J. Mooney, Designing hydrogels for controlled drug delivery. *Nat. Rev. Mater.* **1**, 16071 (2016).
43. B. A. Aguado, J. C. Grim, A. M. Rosales, J. J. Watson-Capps, K. S. Anseth, Engineering precision biomaterials for personalized medicine. *Sci. Transl. Med.* **10**, eaam8645 (2018).
44. K. H. Vining, D. J. Mooney, Mechanical forces direct stem cell behaviour in development and regeneration. *Nat. Rev. Mol. Cell Biol.* **18**, 728–742 (2017).
45. J. Lee, B. L. Zambrano, J. Woo, K. Yoon, T. Lee, Recent advances in 1D stretchable electrodes and devices for textile and wearable electronics: Materials, fabrications, and applications. *Adv. Mater.* **32**, 1902532 (2020).
46. Y. Kim, G. A. Parada, S. Liu, X. Zhao, Ferromagnetic soft continuum robots. *Sci. Robot.* **4**, eaax7329 (2019).
47. H. Yang, C. Li, J. Tang, Z. Suo, Strong and degradable adhesion of hydrogels. *ACS Appl. Bio Mater.* **2**, 1781–1786 (2019).
48. J. Liu, Y. Pang, S. Zhang, C. Cleveland, X. Yin, L. Booth, J. Lin, Y.-A. L. Lee, H. Mazdiyasni, S. Saxton, A. R. Kirtane, T. von Erlach, J. Rogner, R. Langer, G. Traverso, Triggerable tough hydrogels for gastric resident dosage forms. *Nat. Commun.* **8**, 124 (2017).
49. G. G. Adams, M. Nosonovsky, Contact modeling — Forces. *Tribol. Int.* **33**, 431–442 (2000).

Acknowledgments: We acknowledged Life Sciences Complex Advanced BioImaging Facility (ABIF) at McGill University for fluorescence image collection and processing, Prof. N. Tufenkji for equipment support with antibacterial assays, as well as the assistance of A. Skripka with the experimental setup for NIR bioimaging. **Funding:** This work was supported by Natural Sciences and Engineering Research Council of Canada (NSERC, grant RGPIN-2018-04146), Canada Foundation for Innovation (grant 37719) and Fonds de Recherche du Québec–Nature et technologies (FRQNT; grant NC-270740, PR-281851). Z.M. acknowledged the financial support from FRQNT Doctoral Research Scholarship and McGill Engineering Doctoral Award. D.M. was grateful for the financial support from NSERC and FRQNT. **Author contributions:** J.L. and Z.M. conceived the idea and designed the research. Z.M., G.B., A.V., F.Y., R.H., C.W., G.S., and D.M. carried out the experiments. Z.Y. performed the finite element modeling and analysis. Z.M., Z.Y., G.B., A.V., F.Y., Z.-H.G., and J.L. analyzed and interpreted the results. Q.G. and Z.M. performed the in vivo studies. Z.M., Z.Y., Z.-H.G., and J.L. drafted the manuscript, and all authors contributed to the writing of the manuscript. **Competing interests:** The authors declare that they have no competing interests**. Data and materials availability:** All data needed to evaluate the conclusions in the paper are present in the paper and/or the Supplementary Materials. Additional data related to this paper may be requested from the authors.

Submitted 18 April 2020
Accepted 19 February 2021
Published 7 April 2021
10.1126/sciadv.abc3012

Citation: Z. Ma, Z. Yang, Q. Gao, G. Bao, A. Valiei, F. Yang, R. Huo, C. Wang, G. Song, D. Ma, Z.-H. Gao, J. Li, Bioinspired tough gel sheath for robust and versatile surface functionalization. *Sci. Adv.* **7**, eabc3012 (2021).